

# Supplementary Information for Anneal-path correction in flux qubits

Mostafa Khezri,<sup>1,2,\*</sup> Jeffrey A. Grover,<sup>3,\*</sup> James I. Basham,<sup>3</sup> Steven M. Disseler,<sup>3</sup>  
Huo Chen,<sup>1,2</sup> Sergey Novikov,<sup>3</sup> Kenneth M. Zick,<sup>3</sup> and Daniel A. Lidar<sup>1,2,4,5</sup>

<sup>1</sup>*Department of Electrical Engineering, University of Southern California, Los Angeles, California 90089, USA*

<sup>2</sup>*Center for Quantum Information Science & Technology, University of Southern California, Los Angeles, California 90089, USA*

<sup>3</sup>*Northrop Grumman Corporation, Linthicum, Maryland 21090, USA*

<sup>4</sup>*Department of Chemistry, University of Southern California, Los Angeles, California 90089, USA*

<sup>5</sup>*Department of Physics, University of Southern California, Los Angeles, California 90089, USA*

## SUPPLEMENTARY NOTE 1: SPECTROSCOPY DATA AND FIT

Supplementary Figure 1 shows our qubit spectroscopy data (filled circles), and strong agreement between the fitted circuit models and the data.

With all the circuit parameters extracted via fit to spectroscopy data, we can numerically calculate the  $0 \leftrightarrow 1$  transition frequency of the circuit as a function of control biases. The result is shown in Supplementary Figure 2. The qubit gap is a periodic function of the control fluxes, and annealing paths could be chosen from any of the periodic “cells” [Supplementary Figure 2(a)]. The asymmetry extraction procedure discussed in the main text uses one of these cells, which is shown in Supplementary Figure 2(b) for the same flux ranges as in Fig. 3 of the main text. It can be seen that the minimum gap occurs at  $\varphi_z = \varphi_d$  for  $\pi \leq \varphi_x \leq 3\pi$ , indicated by the white dashed line in Supplementary Figure 2(b). Note that at  $\varphi_x = 0$ , the degeneracy occurs at  $\varphi_z = \pi$  (i.e., half flux-quantum).

## SUPPLEMENTARY NOTE 2: PERSISTENT-CURRENT READOUT

The persistent-current readout uses a quantum flux parametron (QFP), which is positioned between the qubit and an rf-SQUID resonator and inductively coupled to both (Fig. 1 of main text). The QFP, which is a larger flux-qubit-like device operated in a classical regime, amplifies the persistent-current signal and isolates the CSFQ from the resonator. This reduces the Purcell effect and increases  $T_1$  [1, 2]. At the end of each anneal, the circulating current in the qubit creates an effective tilt bias on the QFP that changes the direction of its circulating current, which in turn shifts the rf-SQUID resonator frequency that can be measured to infer the direction of the circulating currents.

The persistent-current readout has an effective positive operator valued measure (POVM) for calculating

the probability of measuring the right circulating current, which can be written as

$$\hat{M}_r = \sum_{\lambda} f\left(\frac{I_{\lambda}}{\Delta I}\right) |\lambda\rangle\langle\lambda|, \quad (1)$$

where  $I_{\lambda}$  and  $|\lambda\rangle$  are the eigenvalues and eigenvectors of the persistent-current operator respectively,  $f(x) = [\tanh(x) + 1]/2$  is a filter function, and  $\Delta I$  is the sensitivity of the persistent-current readout device, which in our QFP-based system is  $\Delta I = 10$  nA. The probability of measuring the right circulating current is then  $P_r = \text{Tr}(\rho\hat{M}_r)$ , where  $\rho$  is the qubit density matrix.

## SUPPLEMENTARY NOTE 3: MAPPING CIRCUIT TO ISING SPIN

In order to map the multi-level circuit Hamiltonian into an Ising spin model with only two levels, we keep the two lowest eigenenergies of the CSFQ, as these are the two levels we use for representing a qubit. Furthermore, because we perform a persistent-current measurement at the end of each anneal, we would like the computational basis to be the eigenstates of the persistent-current operator. Therefore, we first write the persistent-current operator in the low-energy subspace as

$$I_p^{\text{low}} = \begin{pmatrix} \langle g|\hat{I}_p|g\rangle & \langle g|\hat{I}_p|e\rangle \\ \langle e|\hat{I}_p|g\rangle & \langle e|\hat{I}_p|e\rangle \end{pmatrix}, \quad (2)$$

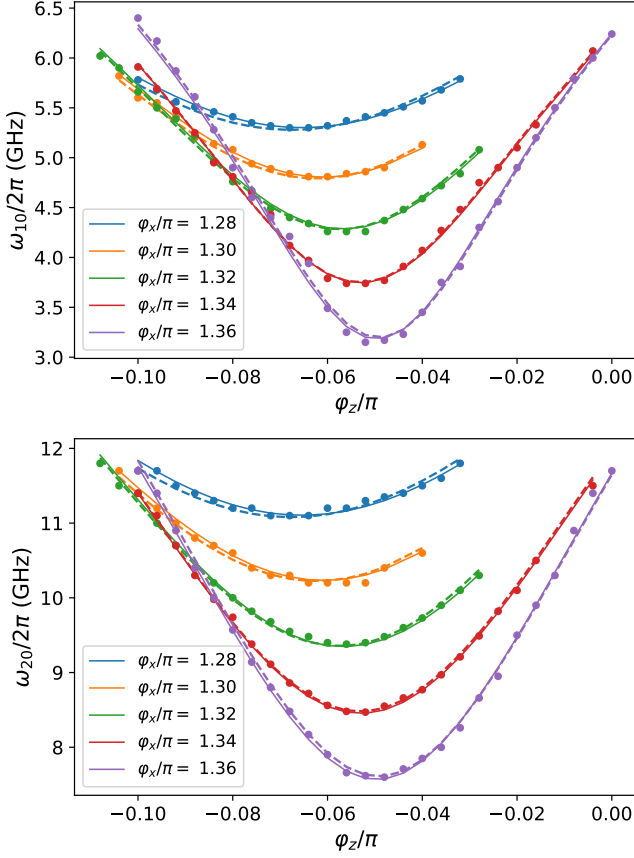
where  $\{|g\rangle, |e\rangle\}$  are the ground and excited eigenstates of the *circuit* Hamiltonian with eigenenergies  $\{E_g, E_e\}$  respectively, and  $\hat{I}_p$  is the persistent-current operator.

Note that for flux qubits where we associate the qubit states to circulating currents flowing in opposing directions, we require the eigenvalues of  $I_p^{\text{low}}$  to have opposite signs. If we tilt the qubit potential beyond a certain point, then the first two eigenstates of the circuit will both be localized in the same well and the eigenvalues of  $I_p^{\text{low}}$  will have the same sign. This puts an upper bound on  $|\varphi_z|$ , which is illustrated in Fig. 2 of the main text.

Now let  $U$  be the unitary basis transformation that diagonalizes  $I_p^{\text{low}}$ , or in other words, transforms the energy basis into the computational (persistent-current) basis.

---

\* These authors contributed equally to this work



Supplementary Figure 1. Fit and experimental spectroscopy data for the  $\omega_{10}$  (top panel) and  $\omega_{20}$  (bottom panel) transition frequencies. Filled circles are qubit resonance frequencies extracted from experimental spectroscopy data. Solid lines are the fit to the 2D qubit model, and dashed lines are the fit to the 1D qubit model. Each color matched band corresponds to a spectroscopic measurement where  $\varphi_x$  was kept fixed and  $\varphi_z$  was swept near the degeneracy point.

$U$  is formed from the eigenstates of  $I_p^{\text{low}}$  as its columns. The computational basis  $\{|0\rangle, |1\rangle\}$  is then

$$\begin{pmatrix} |0\rangle \\ |1\rangle \end{pmatrix} = U^\dagger \begin{pmatrix} |g\rangle \\ |e\rangle \end{pmatrix}, \quad (3)$$

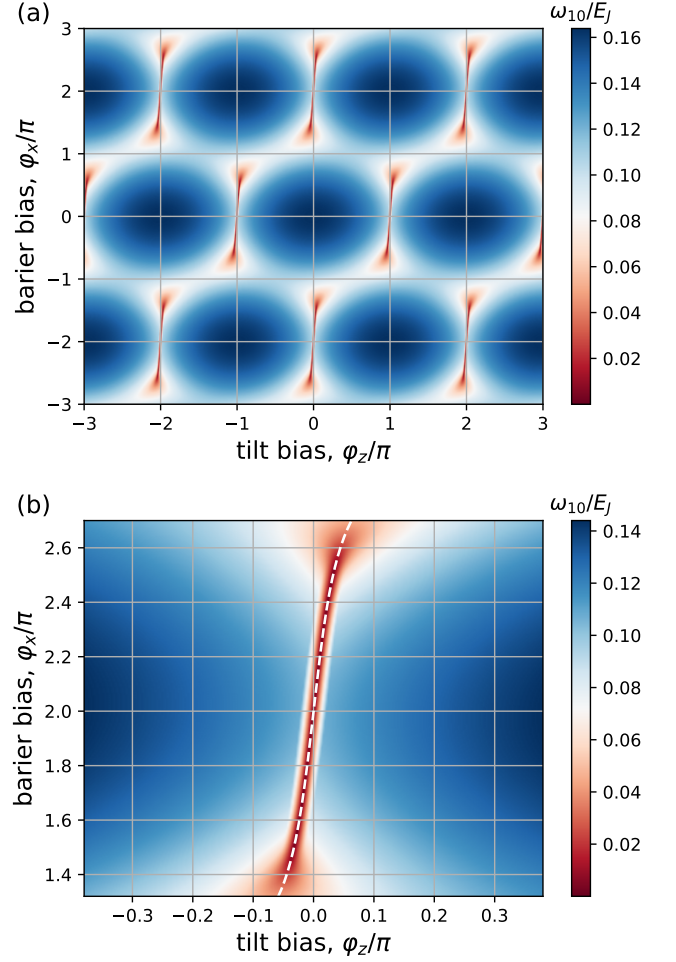
and the effective Hamiltonian in the computational basis is

$$H_{\text{eff}} = U^\dagger \begin{pmatrix} E_g & 0 \\ 0 & E_e \end{pmatrix} U. \quad (4)$$

We extract the Ising coefficients by rewriting the effective Hamiltonian as

$$H_{\text{eff}} = \alpha_x \sigma_x + \alpha_y \sigma_y + \alpha_z \sigma_z + \alpha_I I. \quad (5)$$

For simplicity, the following constraints are usually imposed on the effective Hamiltonian by applying an additional unitary transformation to the computational basis:



Supplementary Figure 2. Gap of the qubit as a function of control fluxes, calculated by diagonalizing the circuit Hamiltonian using the fitted parameters of the circuit, presented in Table II of the main text. For our parameters,  $E_J/2\pi \approx 100$  GHz (a) Periodic structure of the gap, showing multiple “cells”. (b) Zoomed-in gap, with bias ranges that correspond to Fig. 3 of main text that was used for extraction of the asymmetry parameter. White dashed line shows the location of the minimum gap, which occurs at  $\varphi_z = \varphi_d$  for  $\pi \leq \varphi_x \leq 3\pi$ .

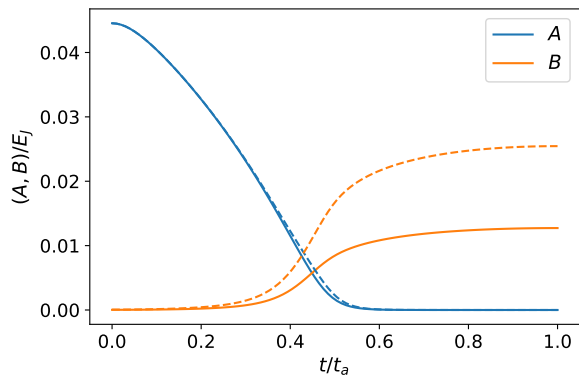
1.  $\alpha_y$  is set to zero.
2.  $\alpha_x$  is always positive.

After imposing the above constraints, we can write the effective Hamiltonian as a standard transverse field Ising Hamiltonian of the form

$$H_{\text{eff}} = A\sigma_x + B\sigma_z. \quad (6)$$

This procedure leads to Fig. 2 in the main text.

As an example, and to make the connection between the s-curve measurements and the qubit picture, we calculate the  $A$  and  $B$  coefficients for two of the asymmetry-corrected anneal paths that were used for the measurements in Fig. 4 of the main text. The result is shown in



Supplementary Figure 3. Transverse field Ising Hamiltonian coefficients for two of the asymmetry-corrected anneal paths, *vs* normalized anneal time  $t/t_a$ . Solid lines correspond to the anneal path with  $\varphi_z(0)/\pi = 0.005$ , dashed lines correspond to the path with  $\varphi_z(0)/\pi = 0.01$ . For our system  $E_J/2\pi \approx 100$  GHz.

Supplementary Figure 3, where the solid lines correspond to the anneal path with  $\varphi_z(0)/\pi = 0.005$ , and the dashed lines correspond to the path with  $\varphi_z(0)/\pi = 0.01$ .

#### SUPPLEMENTARY NOTE 4: EXPERIMENTAL SETUP

Figure 4 is a schematic representation of the measurement setup from room temperature down to the mixing chamber. The experiments are performed in a Leiden Cryogenics dilution refrigerator, with a base temperature in the range of 15 – 25 mK. Slow flux biases are provided by independent arbitrary waveform generator (AWG) channels and reach the device via phosphor-bronze ribbon cables from 300 K to 4 K, followed by NbTi cables from 4 K to the mixing chamber. Fast control is provided by different, independent AWG channels that utilize their full 1 GS/s time resolution. These fast biases are sent down coax lines, and they are combined with the slow biases at the mixing chamber via cryogenic bias-tees with an added 1-GHz low-pass filter. Output signals are first amplified by a Josephson traveling-wave parametric amplifier (JTWPA) [3] at the mixing chamber, followed by a high-electron-mobility transistor (HEMT) amplifier anchored at 4 K.

For readout we use a split-heterodyne configuration with image rejection to downconvert signals into the intermediate frequency (IF) band, typically 50 MHz. A field programmable gate array (FPGA) digitizer performs analog-to-digital conversion for signal processing and analysis. A simple boxcar windowing function is applied for IF demodulation [4], which is done either directly on the FPGA or in software after the full signal traces are transferred off the card.

Details of the device layout and fabrication can be

found in the Appendix of Ref. [2].

#### SUPPLEMENTARY NOTE 5: LIFETIME AND COHERENCE

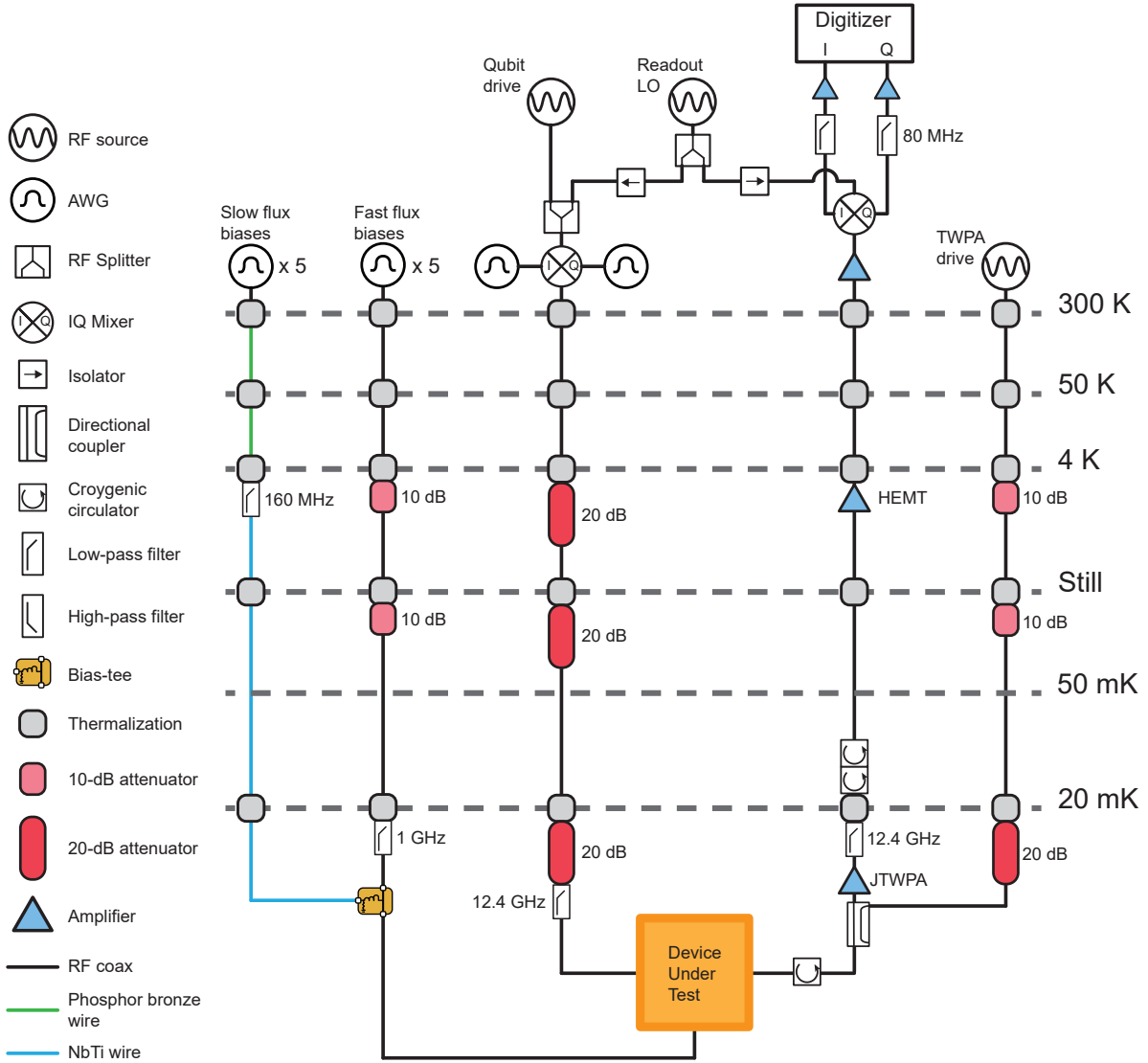
Figure 5 presents a characteristic lifetime measurement of the qubit at a transition frequency of 5.9 GHz. Repeated measurements yield an average value of  $T_1 = 1.93 \pm 0.19 \mu\text{s}$  ( $1\sigma$  error). We have confirmed that qubit lifetime remains roughly constant over a range of qubit frequencies of about 1 GHz around this measurement, but it is expected that lifetime will decrease as the gap closes [5]. Using Ramsey interferometry, we measured a dephasing time of  $T_2^* = 130$  ns at a qubit frequency of 4.2 GHz in a similar device (four-junction CSFQ with the same design  $I_p$ ) from the same fabrication run [6].

We note that  $T_1$  is affected by a combination of slow flux noise, fast charge noise, and Purcell decay through the readout resonator, and the qubit dephasing time (and therefore  $T_2$ ) can be adversely affected by the shot noise of residual photons in the dispersive resonator. In general, as the qubit gap becomes small, the slow flux noise becomes dominant and degrades the energy relaxation time with a scaling of  $1/I_p^2$  and the coherence time with a Gaussian decay scaling of  $1/I_p$ . At large qubit frequencies the fast charge noise takes over and degrades the lifetime, although it is sometimes challenging to distinguish it from fast flux noise [7]. Additionally, as the detuning between the qubit and the readout resonator becomes small, the qubit lifetime degrades due to an increase in the Purcell decay [8].

The interplay between all these effects on CSFQs was extensively studied in Ref. [7], where the coherence times and their main contributing factors varied depending on different qubit operating regimes and system parameters. A similar systematic study of coherence in the present system was beyond the scope of our work. Nevertheless, due to the similarity in CSFQ design and parameters and fabrication, we expect similar results to those of Ref. [7].

#### SUPPLEMENTARY NOTE 6: THE EFFECT OF IDLING POST ANNEAL

As illustrated in Fig. 5 of the main text, peaks in the s-curve appear when the anneal path traverses level crossings, leading to diabatic population transfer. The AME simulations reproduce these peaks only when an idle time is added between the end of the qubit anneal and readout. Without any delay, the theory predicts that instead the s-curve will exhibit plateaus. This delay allows for relaxation to occur, redistributing population between levels in either well. However, note that the AME with an Ohmic bath produces large transition rates at small gaps [9], which means the peaks will rise faster than they do in the experiment. Nevertheless, the AME can qualita-



Supplementary Figure 4. A schematic diagram of the room-temperature measurement setup and dilution refrigerator wiring.

tively predict the effect of an idle time after the anneals, as seen in Supplementary Figure 6 and Fig. 5(a) of the main text.

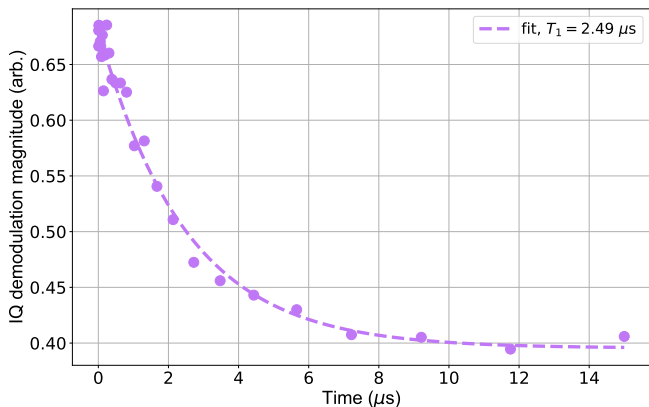
We confirm this effect experimentally by varying the idle time after the anneals, as shown in Supplementary Figure 6. The anneal is depicted in Fig. 3 of the main text, where the anneal traverses a “tilted” path in flux space due to a large amplitude applied to the tilt bias. As the idle time increases from 2 ns to 600 ns, plateau-like features in the s-curve become peaks, as expected from the theory.

We performed similar delay studies with asymmetry-corrected anneal paths, and neither the plateaus nor the peaks appeared (not shown). This suggests that fewer excitations into higher-energy states occurred.

## SUPPLEMENTARY NOTE 7: EXPERIMENTAL PULSES

In this section we describe in more detail the actual pulses used to perform the correction, as well as how different pulse parameters affect the s-curve width.

Note that for experimental parameters, we use real flux values in units of  $\Phi_0$ , and recall the relation to phase:  $\varphi_{x,z} = 2\pi\Phi_{x,z}/\Phi_0$ . As implied by Eq. (2) in the main text, we parametrize the  $z$ -flux in terms of the  $x$ -flux. We first decide on a functional form and duration for  $\Phi_x(t)$ , and then Eq. (2) is used to determine  $\Phi_z(t)$  from those values of  $\Phi_x$ . We found that a gaussian pulse shape for the  $x$ -flux produced better results than a linear ramp, likely due to reduced pulse distortion in the RF-coax lines. Future studies could explore using more sophis-



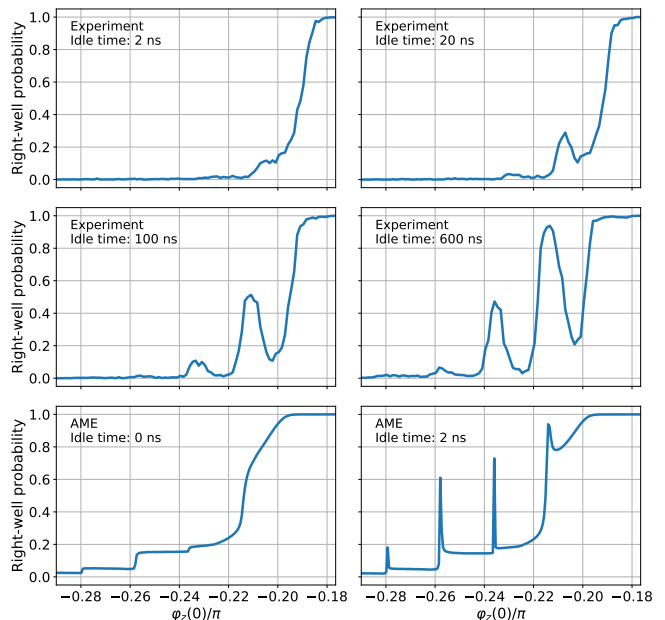
Supplementary Figure 5. One realization of an energy relaxation measurement of the qubit at a frequency of 5.9 GHz. The plot uses IQ demodulation amplitude on the y-axis, which is proportional to excited-state population. The fit (dashed purple line) is a simple exponential decay model, and we obtain a lifetime of  $2.49 \mu\text{s}$  for this dataset.

ticated techniques, such as DRAG [10] or optimal control [11], to find more performant pulses.

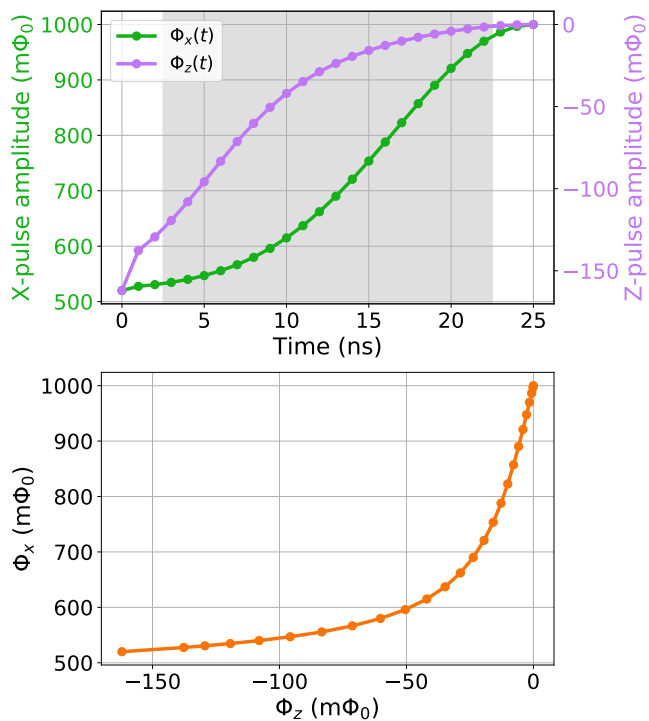
Figure 7 illustrates the pulses used to correct for an asymmetry of  $d = 0.102$ . The top plot shows each independent control line as a function of time. The shaded gray area indicates the 5 – 95% rise time of 20 ns, which is the parameter used when defining the “anneal time” for a particular experiment. The bottom plot then combines these two pulse to illustrate the actual annealing path traversed by the qubit. The displayed pulse shapes are as-measured at the outputs of the 1 GS/s arbitrary waveform generators (AWGs). In this study, no pulse distortion correction was applied [12, 13], but it will be part of future experimental improvements.

We also studied the effect of changing the value of  $d$  when applying the correction. Supplementary Figure 8 highlights the reduction in s-curve width when the value of  $d$  is near the value of  $\approx 0.102$  measured during calibration (and verified in simulation). The difference in trends between the two anneal times suggests that there is potentially more room for optimization by exploring the entire space of annealing time in addition to the path trajectory.

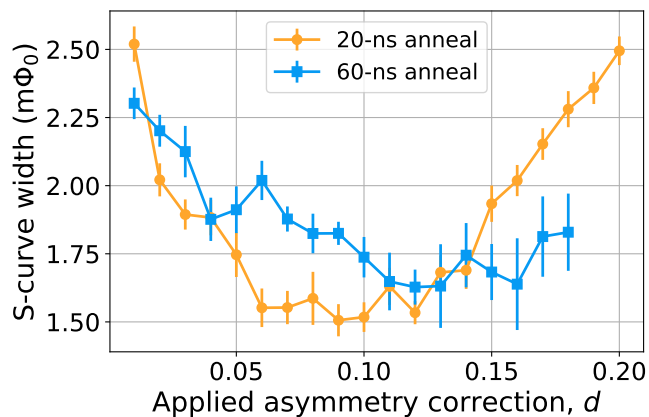
We also note that the data in Supplementary Figure 8 were taken when the fridge base temperature was 20% higher (24 mK) than that in the main text (20 mK). This accounts for the overall increase in measured s-curve widths.



Supplementary Figure 6. The effect of post-anneal idle time on s-curve characteristics. The anneal is similar to the one described in Fig. 5 of the main text: the anneal occurs in 60 ns, with an amplitude of  $0.33\pi$  applied to the tilt bias. From left-to-right and top-to-bottom, the first four panels show the experimental results when the idle time before readout is increased from 2 ns to 600 ns. The last two panels show the effect of idle time in AME simulations. The fast rise of the peaks in AME simulations is expected (see the text).



Supplementary Figure 7. Experimental pulses used to correct for junction asymmetry of magnitude  $d = 0.102$ . Top:  $x$  [ $\Phi_x(t)$ , green circles] and  $z$  [ $\Phi_z(t)$ , purple circles] flux pulses at the outputs of the AWGs as a function of time. The hitch after the first point is due to truncation of the gaussian pulse, and can be smoothed in software. The gray shaded area indicates the 20 ns rise time. Bottom: The corrected pulse visualized in flux space, where each orange circle corresponds to one time step from the top plot.



Supplementary Figure 8. S-curve width versus applied correction parameter for two different anneal times of 20 ns (orange circles) and 60 ns (blue squares).

- 
- [1] J. Strand *et al.*, “High Coherence Quantum Annealing and Fast, High-Fidelity Flux Qubit Readout,” Invited presentation at ISEC, Riverside, USA, July 2019.
- [2] J. A. Grover *et al.*, “Fast, lifetime-preserving readout for high-coherence quantum annealers,” *PRX Quantum* **1**, 020314 (2020).
- [3] C. Macklin *et al.*, “A near-quantum-limited josephson traveling-wave parametric amplifier,” *Science* **350**, 307–310 (2015).
- [4] P. Krantz, M. Kjaergaard, F. Yan, T. P. Orlando, S. Gustavsson, and W. D. Oliver, “A quantum engineer’s guide to superconducting qubits,” *Appl. Phys. Rev.* **6**, 021318 (2019).
- [5] C. M. Quintana *et al.*, “Observation of classical-quantum crossover of  $1/f$  flux noise and its paramagnetic temperature dependence,” *Phys. Rev. Lett.* **118**, 057702 (2017).
- [6] S. Novikov *et al.*, “Exploring More-Coherent Quantum Annealing,” in *IEEE International Conference on Rebooting Computing (ICRC)* (McLean, VA, USA, 2018) p. 1.
- [7] F. Yan *et al.*, “The flux qubit revisited to enhance coherence and reproducibility,” *Nat. Commun.* **7**, 12964 (2016).
- [8] A. Blais, R.-S. Huang, A. Wallraff, S. M. Girvin, and R. J. Schoelkopf, “Cavity quantum electrodynamics for superconducting electrical circuits: An architecture for quantum computation,” *Phys. Rev. A* **69**, 062320 (2004).
- [9] T. Albash and D. A. Lidar, “Decoherence in adiabatic quantum computation,” *Phys. Rev. A* **91**, 062320 (2015).
- [10] F. Motzoi, J. M. Gambetta, P. Rebentrost, and F. K. Wilhelm, “Simple pulses for elimination of leakage in weakly nonlinear qubits,” *Phys. Rev. Lett.* **103**, 110501 (2009).
- [11] M. Werninghaus, D. J. Egger, F. Roy, S. Machnes, F. K. Wilhelm, and S. Filipp, “Leakage reduction in fast superconducting qubit gates via optimal control,” (2020), [arXiv:2003.05952 \[quant-ph\]](https://arxiv.org/abs/2003.05952).
- [12] S. Gustavsson *et al.*, “Improving quantum gate fidelities by using a qubit to measure microwave pulse distortions,” *Phys. Rev. Lett.* **110**, 040502 (2013).
- [13] M. A. Rol *et al.*, “Time-domain characterization and correction of on-chip distortion of control pulses in a quantum processor,” *Appl. Phys. Lett.* **116**, 054001 (2020).